Proceedings of ASME Turbo Expo 2023
Turbomachinery Technical Conference and Exposition
GT2023
June 26-30, 2023, Boston, Massachusetts, USA

GT2023-102824

AN EXPERIMENTAL STUDY OF THE STABILITY AND NEARFIELD STRUCTURE OF OXYFUEL JET FLAMES AT ELEVATED PRESSURES

Muhammad Bukar
King Abdullah University of Science and Technology
Thuwal, Saudi Arabia

Suman Basnet
King Abdullah University of Science and Technology
Thuwal, Saudi Arabia

Bin Wu
King Abdullah University of Science and Technology
Thuwal, Saudi Arabia

Gaetano Magnotti
King Abdullah University of Science and Technology
Thuwal, Saudi Arabia

ABSTRACT

This study presents experimental results of the stability limit and the nearfield structure of oxy-methane jet flames at pressures ranging from 2- 5 bar. The oxidizer used in this campaign consists of 40% O_2 and 60% CO_2. Two sets of cases were studied: one where pressure increase was achieved by keeping the fuel Reynolds number constant and the other where the velocity was kept constant while increasing pressure. Stability limits (lift-off velocity) are reported for various coflow velocities at different operating pressures. Natural flame luminosity imaging with a DSLR camera and combined CH chemiluminescence using an ICCD (PIMAX 4) are used to characterize the nearfield structure of the flame. The CH* results were then processed to extract the attachment location, defined in terms of attachment height and radius. The study mainly investigates the effect of pressure on the flame attachment height and radius. The DSLR images complement the study with qualitative information on the flame appearance and sooting propensity. Results show that at constant Reynolds number, the attachment height decreases with pressure for all cases considered while the attachment radius increased with pressure increase. At constant velocity, however, both the attachment height and radius were observed to decrease with increased pressure.*

Keywords: oxyfuel, high pressure, combustion.

NOMENCLATURE

CH_4	Methane
CO_2	Carbon dioxide
O_2	Oxygen
NO	Nitric oxide
U_{fuel}	Fuel jet velocity
U_{coflow}	Coflow velocity
U_L	Lift-off velocity
S_L	Flame propagation velocity
H_L	Flame lift-off height
H_a	Flame attachment height
R_a	Flame attachment radius
D	Outer diameter of the fuel tube

1. INTRODUCTION

Oxyfuel combustion[1] at high pressures is considered one of the most promising carbon capture technologies (CCT), which has the potential to reduce emissions (both CO_2 and NOx) while at the same time increasing the thermodynamic efficiency of the system. It involves burning fuel in pure oxygen (obtained from an Air Separation unit or ASU) at high pressures in a CO_2-enriched environment. The main drawback of oxy-combustion lies in the ASU, which can be quite energy intensive[2]. Two of the leading oxy-combustion-based technologies are the NET power Allam cycle[3] and the semi-closed oxy-combustion combined cycle[4], which both recycle CO_2 at high pressure.

Chemiluminescence imaging of some radicals such as OH* and CH* is used widely in combustion research. Chemiluminescence refers to the phenomenon of light emission by chemically excited molecules returning to their ground state. It is a cheap, non-intrusive technique that can be used to obtain useful information on heat release[5, 6], equivalence ratio[7-9], and reaction zone[10-12]. In hydrocarbon flames, CH* and OH* produce the strongest chemiluminescent intensity peaks at 431nm ($A^2\Delta - X^2\Pi$) and 309 nm ($A^2\Sigma^+ - X^2\Pi$) respectively.

CH* chemiluminescence exists in a thin region of the high-temperature zone and is a good marker of the flame location [13]. In this study, CH* chemiluminescence technique is used to look closer at the mechanism of stabilization in non-premixed oxyfuel jet flames, focusing on the role of pressure on the attachment location and the detachment velocities of these flames.

Flame stabilization in attached and lifted jet flames has been the subject of many studies [14-24]. For lifted flames, the stabilization location is widely recognized to occur at the leading- edge on the stoichiometric contour where the jet axial velocity balances with the flame propagation velocity[25, 26]. This assumes partial-premixing of the gases downstream of the stabilization point. For attached flames as well, a degree of partial premixing is assumed to occur in the "dark region" close to the fuel tube, enabling the flame to stabilize just above the fuel tube. The stabilization location is usually reported in terms of the attachment height, H_a (or H_L for lifted flames), and attachment radius, R_a.

In a previous paper[27], we reported the effect of the O_2/CO_2 ratio in the coflow on the attachment location of oxyfuel jet flames at atmospheric pressure. It was found that both H_a and R_a were larger with higher CO_2 in the oxidizer. Marin et al. [28] reported H_a and R_a values in CH_4/air jet diffusion flames. They found that as methane jet velocity is increased, H_a increases and R_a decreases, and the change in R_a is more significant than that of H_a. They also noticed that the effect of U_{coflow} on the stabilization location is negligibly small. Lamige et al.[18] reported flame stabilization location for eight different burner materials. Depending on the momentum ratio between the fuel and the oxidizer ($MR=\rho_{fuel} U^2_{fuel}/ \rho_{ox}U^2_{ox}$), they identified three main different regimes of stabilization. Colson et al. studied the effect of fuel-side dilution with ammonia and found that with the diluent addition, H_a increases while R_a decreases.

Most of these previous studies have been conducted at atmospheric pressures and the role of pressure has not been duly explored. This work aims to describe the lift-off stability limit and the attachment location of oxyfuel flames at elevated pressures up to 5 bar. The oxidizer stream consists of 40% oxygen and 60% carbon dioxide in volume, while the fuel is pure methane.

2. EXPERIMENTAL SETUP AND METHODS

The experiments in this work were conducted inside the High-Pressure Vessel (HPV) available at the clean combustion research center at KAUST. The vessel is capable of operating at a maximum pressure of 40 bar. Figure 1 shows the schematic of the HPV, the coflow burner, and other components mounted on the HPV to ensure its operation. HPV has four windows of different sizes that allow for both line of sight and 90 degrees scattering measurements. The vessel is oriented vertically to avoid buoyancy-induced asymmetries on the jet flames. A backpressure regulator and pressure relief valve are mounted on the top of the upper flange of the HPV for pressure control and overall operational safety. Air is continuously supplied to charge the vessel to the desired pressure and also to reduce the temperature of the burned gases that go through the back pressure regulator.

The burner inside the HPV is a jet flame burner with the fuel nozzle inner and outer diameters (D) 1.75 mm and 3.18 mm, respectively. The fuel tube and the oxidizer co-flow are enclosed in a 25 mm x 25 mm quartz confinement. A larger optical enclosure (40 mm x 40 mm cross-section and 200 mm tall) surrounds the dilution stream. More details on this burner can be found in ref[27]. All the gas flow rates were controlled using thermal mass flow controllers (Bornkhost) calibrated using a Drycal flow calibrator with an accuracy of 3%. An Nd: YAG laser (Q smart 850), with a maximum energy of 850 mJ at its fundamental wavelength (λ= 1064 nm), was used as the laser source to ignite the flames. The laser beam is expanded, collimated, and focused to a point just above the fuel tube to achieve an ignition-inducing spark.

The attachment height and radius were obtained by post-processing the CH* chemiluminescence images. This signal was obtained using an ICCD camera(Princeton Instruments PIMAX 4) equipped with a 105 mm UV lens (f# 4.5) and a narrow band-pass filter (430 nm± 10 nm) to strengthen the relative contribution of CH* over CO_2* background signal. The CH* images have a pixel resolution of 0.029 mm/pixel. For each flame condition, 200 instantaneous images were acquired with a gate width of 3ms and a gain of 70. These images were first background subtracted and then subjected to the Abel deconvolution method[27] to obtain two-dimensional images. After that, the Canny Edge detection algorithm[29] was used to characterise the boundary of the CH*, from which, the attachment height and radius were determined.

Table 1 shows the test conditions used for the constant velocity cases. The pressure range investigated for this study was 2 bar<P< 5 bar while the coflow velocity considered was fixed at U_{coflow}= 0.60 m/s. The main parameters of interest were then the pressure and U_{fuel}. The operating conditions for the constant Reynolds number cases are shown in Table 2.

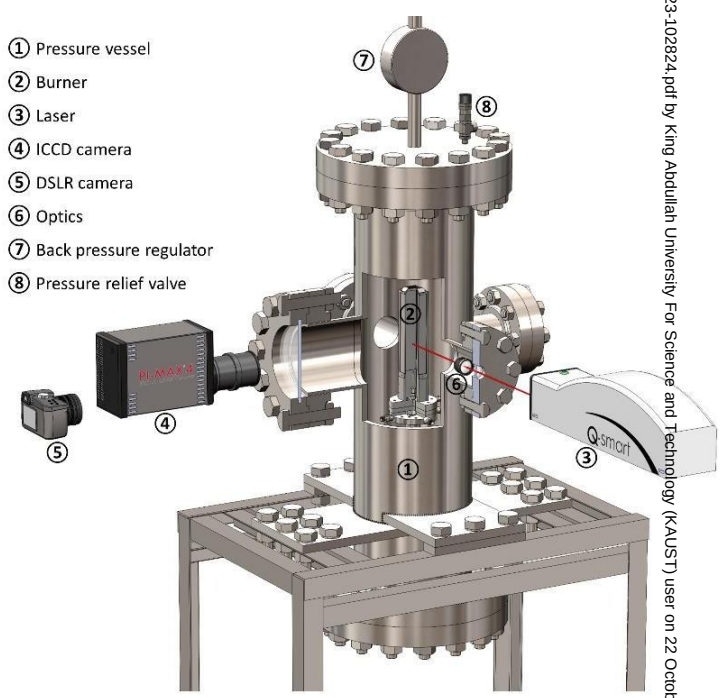

FIGURE 1: Schematic of Experimental setup

Pressure [bar]	Fuel velocity [m/s]	Coflow velocity [m/s]	Laminar burning velocity [m/s]
2	18,20,23,25,28,30,33	0.60	0.36
2.5	18,20,23,25,28,30,33		0.34
3	23,25,28,30		0.32
3.5	23,25,28,30		0.30
4	23,25,28,30		0.29
4.5	23,25,28,30		0.28

Table 1. Operating conditions for the constant velocity cases

Conditions	2 bar	2.5 bar	3 bar	3.5 bar	4 bar	4.5 bar
U_{fuel} [m/s]	38	30	25	21	19	17
U_{coflow}[m/s]	0.86	0.70	0.58	0.50	0.44	0.39

Table 2. Operating conditions for the constant Reynolds number cases rounded to two significant figures.

3. RESULTS AND DISCUSSION

3.1 Effect of pressure on the stability of oxyfuel flames.

Figure 2 shows the lift-off velocities as a function of coflow velocity at different pressures. The black, red, and blue curves represent the lift-off curves at 2, 3, and 4 bars, respectively. For all the cases, the flames lift first and then blow out from a lifted state with increasing U_{fuel}. At each pressure, it can be observed that increasing the coflow velocity reduces the U_L slightly. This coflow dependence partially comes from the contribution of the coflow to the bulk flow velocity. As pressure increases, the detachment velocities of the oxy-flames decrease, hence narrowing the stability range. As the pressure increases, the S_L of the mixture decreases. This quantity is crucial to the stabilization location, as explained in the introduction section.

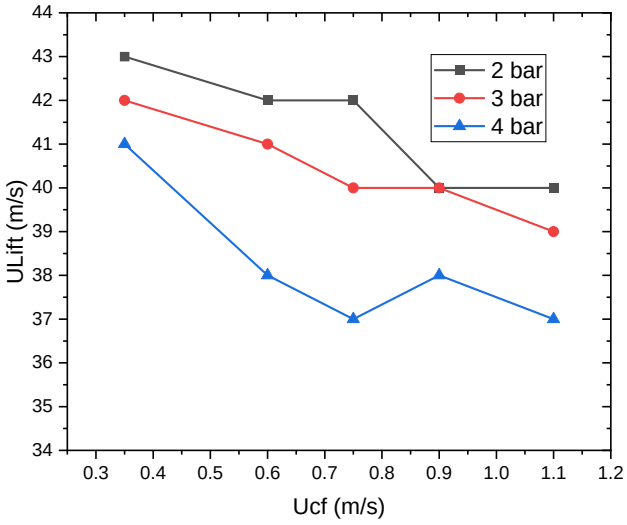

FIGURE 2: Plot of flame detachment velocity as a function of U_{coflow} and pressure.

Figure 3 shows direct images of flames at a pressure range from 2 bar to 5 bar. In figure 3 a), the 2 bar flame appears bluish at the nearfield region (i.e., y/D is small) but changes to bright orange color along the flame, indicating the presence of soot. As the pressure is increased, the bluish region in the nearfield begins to diminish, and at 5 bar, we see that the flame luminosity across the entire length of the flame is greatly increased relative to the 2 bar case. This is indicative of increased soot yield caused by the higher pressures, as was observed in several studies [30-33]. Previous studies have shown a power law dependence of P^n of soot on pressure. The "n" value can change depending on the fuel type and the pressure range being looked at. For example, for laminar CH_4 diffusion flames, the "n" value was 2 for the pressure range between 5 bar and 20 bar[34]. In figures 3 b) and 3 c), we notice the same trend of overall soot luminosity increase as pressure goes from 2 bar to 5 bar. However, the ability of the pressure to increase the soot seems to be attenuated at higher velocities. Figure 3 also shows that at each pressure, when the U_{fuel} increases, the blue region in the flame enlarges, indicating soot reduction. The increased mixing caused by the increase in the U_{fuel} causes the soot production to be localized to the downstream region of the flames

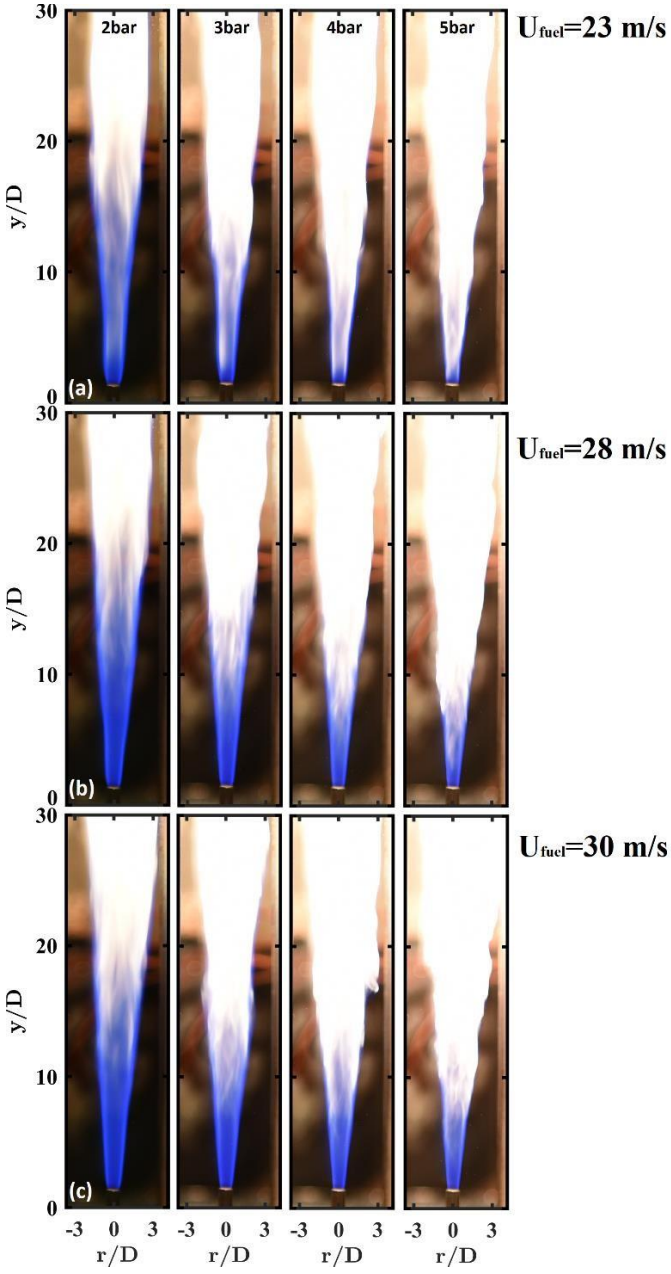

FIGURE 3: Direct images of attached flames (1/100 sec exposure time) for various pressures at fixed fuel and coflow velocities. For example, figure 3 b) (i.e., row 2) shows flames at U_{fuel}=28 m/s and U_{coflow}=0.6 m/s for pressures ranging between 2 bar and 5 bar. The pressures for each case are shown in black on top of each column.

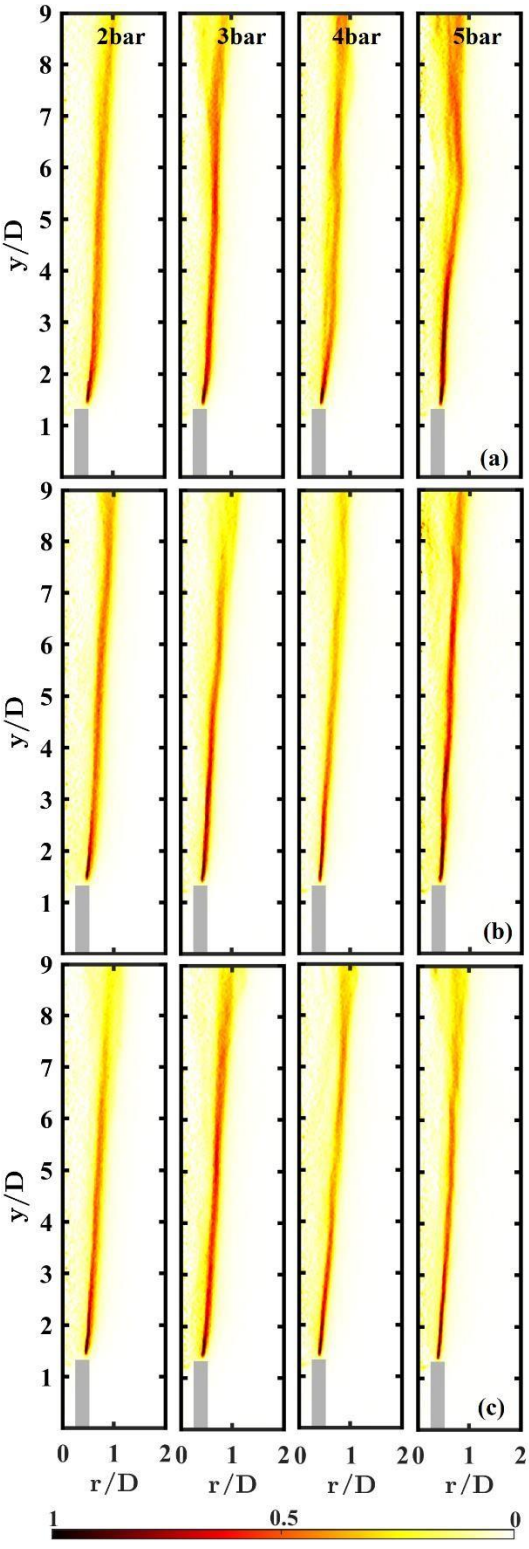

FIGURE 4: CH* chemiluminescence images of the flame test cases shown in fig. 3. The right side of the CH* image is shown here.

3.2 Effect of pressure on the attachment location.

Figure 4 shows the CH* chemiluminescence images obtained using the 430 nm filter. These images correspond to the same conditions, whose direct images with a DSLR camera are shown in fig.3. The mean H_a and R_a were determined from these images. H_a refers to the distance between the bottommost point of the CH* edge and the top of the fuel nozzle, while R_a is the distance between the fuel tube centerline and the lowermost point detected by our edge detection algorithm (see fig. 7).

Constant Velocity cases

Figure 5 shows the plot of the attachment height as a function of U_{fuel} and pressure. The coflow velocity was fixed at 0.6 m/s. The figure shows a general decrease in both H_a and R_a as fuel jet velocity is increased. This dependency holds true for all the pressures tested between 2 to 4.5 bar.

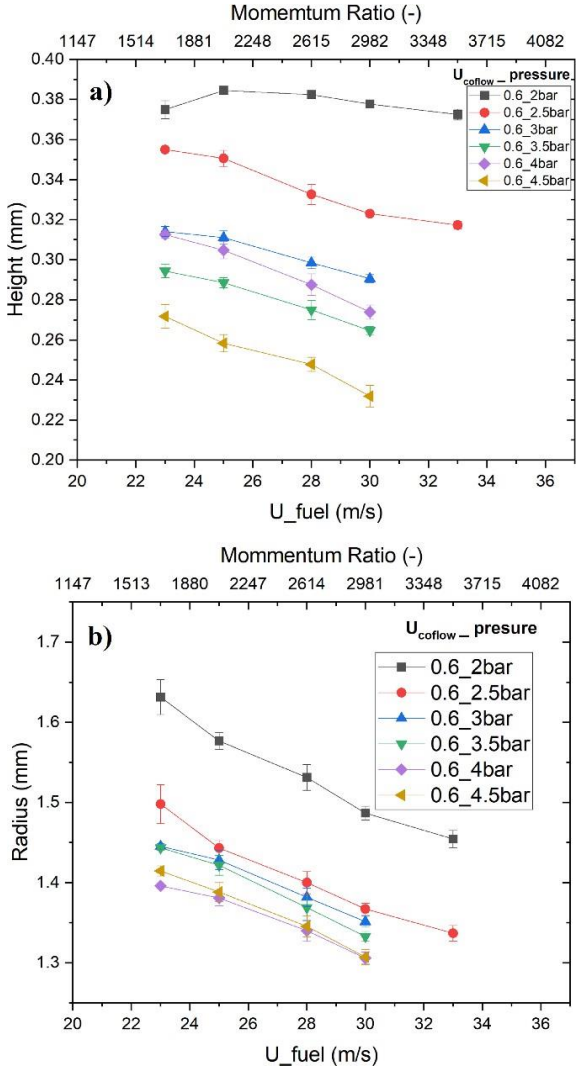

FIGURE 5: Plot a) H_a and b) R_a as a function of U_{fuel} at various pressures. Error bars shown represent the standard deviation.

The decrease in radius can be attributed to the fact that at higher U_{fuel} values, a slimmer stoichiometric contour should be expected due to relatively slow molecular diffusion, and hence the attachment radius decreases.

Previous work from Lamige et al. [18] identifies three main regimes of stabilization depending mainly on the Momentum ratio between the jet and the coflow. In regime I, as the jet MR increases, the flame moves toward the oxidizer (R_a increases) and toward the burner (H_a decreases). Further increasing the MR, the increased oxidizer entrainment moves the stoichiometric contour (where Z = Zst) closer to the burner centerline (R_a decreases) and away from the burner rim (H_a increases).

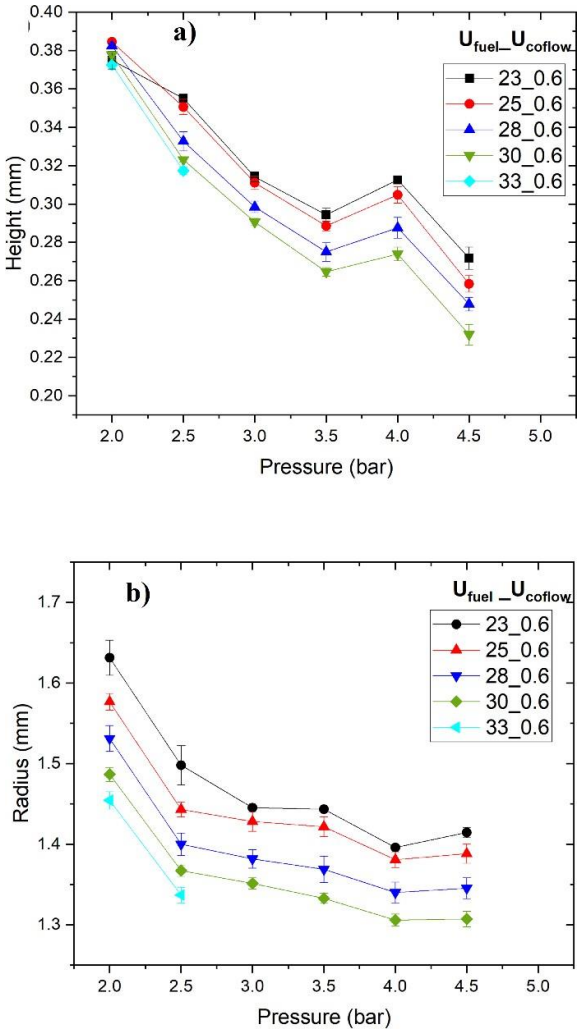

FIGURE 6: Plot a) H_a and b) R_a as a function of Pressure for various jet velocities. Error bars shown represent standard deviation.

Further increasing MR, a third regime is identified, characterized by a decrease in R_a and a small decrease in H_a. The authors showed that for MR~<10, the flame is stabilized according to Regime I, and for momentum ratios>~1000, the flame is stabilized in Regime III. As shown in fig. 5, the momentum ratio range for the cases we studied falls between~1700 <MR<~3500, corresponding to regime III. Our results are consistent with what was observed by both Lamige et al. [18] and Colson et al.[35].

To look more closely at the effect of pressure, we plotted H_a and R_a as a function of pressure in fig.6. Each curve corresponds to fixed fuel and coflow velocities. It can be seen from the plot that as pressure goes up, the flame stabilizes closer to the burner rim in both axial and radial directions. The reduction in R_a with pressure can again be explained by its effect on the jet spreading angle. At fixed velocity, the Reynolds number scales with pressure. This Reynolds number increase narrows the jet and moves it close to the centerline. The location of flame stabilization is determined by the point at which the local flow speed is matched by the flame propagation velocity. When the pressure increases, S_L decreases as shown in table 1. However, with increased pressure, other parameters, such as the flame temperature, could also play a role in determining the stabilization location. Even though the bulk velocities are fixed, the local axial velocity at the stabilization location could be affected by pressure.

Constant Reynolds Number cases.

Figure 8 shows the Direct Images using DSLR for the constant Reynolds number cases. In this series, as pressure was increased, the volumetric flow rates of the gases were kept constant instead of the velocities. In other words, the velocities decreased with increased pressure. We see from fig.8 that as pressure increases, the sooting propensity of the flames also increases, as evidenced by the rapid diminishing of the blue region on the flames. It is also quite visible that as the pressure increases, the buoyancy effect on the flame becomes more evident. A general decrease in the flame length was also observed, although it is not a focus of this study.

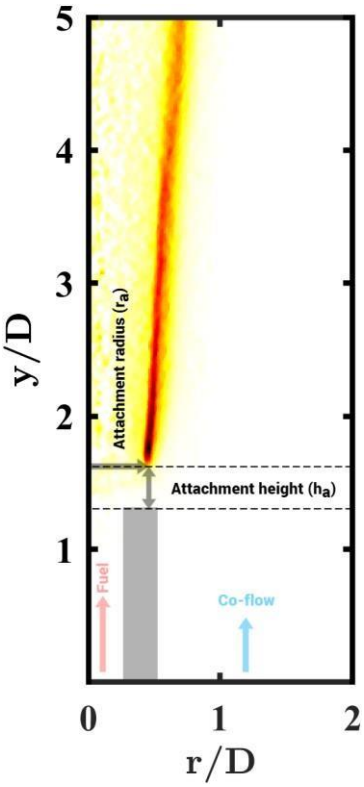

FIGURE 7: Illustration of the definitions of attachment height and radius used.

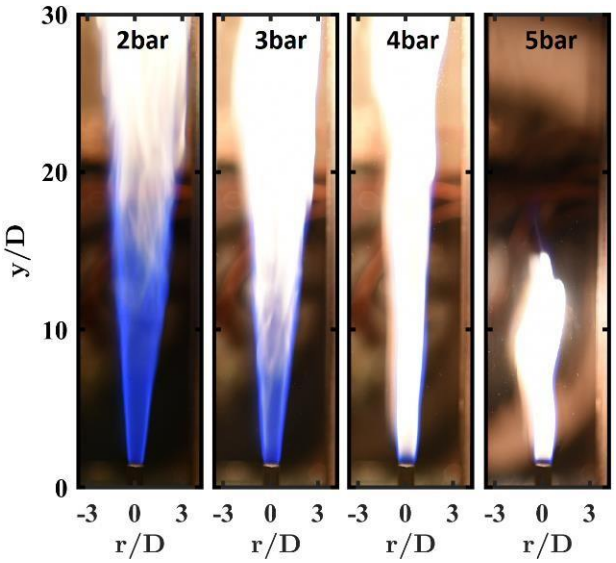

FIGURE 8: Direct DSLR images of oxyfuel flames at various pressures. The U_{fuel} and U_{coflow} for these flames are given in Table 2.

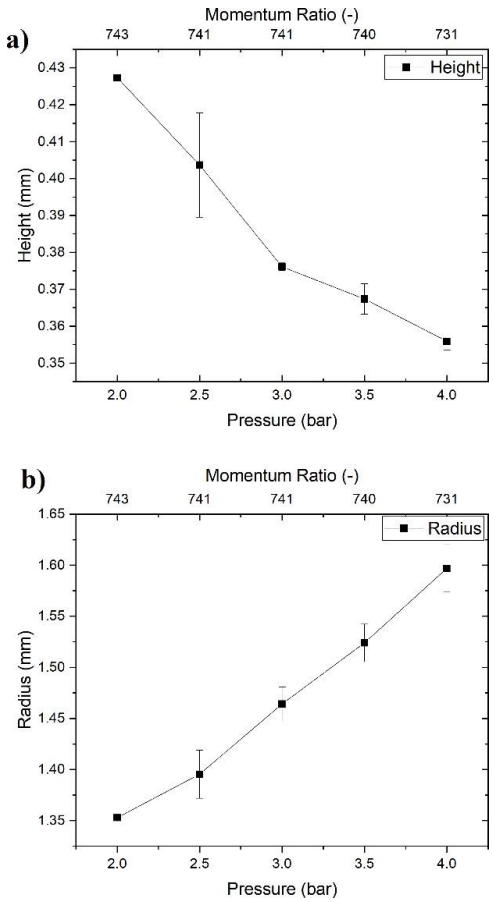

FIGURE 9: Plot a) H_a and b) R_a as a function of pressure and Momentum ratio (on the top) at constant Reynolds number. Error bars shown represent standard deviation.

Figure 9 shows a plot of attachment height and radius as a function of pressure for the constant Reynolds number cases mentioned in table 2. The figure shows that H_a decreases with pressure while R_a increases. As pressure increases, the velocities decrease because we keep the volumetric flow rates constant. This decrease in the flow velocities means that the mixture S_L dominates the incoming local flow and causes the flame to stabilize close to the fuel tube. When we look at the range of the momentum ratio, we notice that we are in the second regime of stabilization identified by references [18, 35], and our results are consistent with what was observed in those studies.

4. CONCLUSION

A new high-pressure vessel was used to experimentally investigate a series of oxyfuel jet flames at elevated pressures. The stability limit of these flames was reported at various elevated pressures, and DSLR and CH* chemiluminescence images of the attached flame conditions were acquired. The CH* images were processed to investigate the effect of pressure on the stabilization location. It was found that as pressure is increased while keeping gas velocities constant, the flame stabilization location moves closer to the tube(i.e., lower H_a) and closer to the burner center line(lower R_a) before it eventually blows off. But if the pressure increase was achieved by lowering the velocities while keeping the gas flow rates constant, the attachment radius is increased while the attachment height is decreased. Observations were also made on the effect of elevated pressure on the sooting propensity of these attached flames. An overall increase in soot yield was observed with increasing pressure for both the constant velocity and constant Reynolds number cases.

ACKNOWLEDGEMENTS

The authors want to acknowledge that this work was funded by the clean combustion research center at King Abdullah University of Science and Technology (KAUST).

REFERENCES

[1] X. Huang, J. Guo, Z. Liu, C. Zheng, Opportunities and challenges of oxyfuel combustion, in: Oxyfuel Combustion, Elsevier, 2018, pp. 1-12.
[2] A. Darde, R. Prabhakar, J.-P. Tranier, N. Perrin, Energy Procedia, 1 (1) (2009) 527-534.
[3] R. Allam, S. Martin, B. Forrest, J. Fetvedt, X. Lu, D. Freed, G.W. Brown Jr, T. Sasaki, M. Itoh, J. Manning, Energy Procedia, 114 (2017) 5948-5966.
[4] M. Sammak, M. Thern, M. Genrup, in: Turbo Expo: Power for Land, Sea, and Air, American Society of Mechanical Engineers, 2018, pp. V003T006A010.
[5] A. Hossain, Y. Nakamura, Combust. Flame, 161 (1) (2014) 162-172.
[6] Y. Hardalupas, C. Panoutsos, A. Taylor, Exp. Fluids, 49 (4) (2010) 883-909.
[7] Y. Hardalupas, M. Orain, C.S. Panoutsos, A. Taylor, J. Olofsson, H. Seyfried, M. Richter, J. Hult, M. Aldén, F. Hermann, Appl. Therm. Eng., 24 (11-12) (2004) 1619-1632.
[8] F. Quintino, T.P. Trindade, E.C. Fernandes, Fuel, 231 (2018) 328-340.
[9] M. Orain, Y. Hardalupas, Comptes Rendus Mecanique, 338 (5) (2010) 241-254.
[10] J. Kojima, Y. Ikeda, T. Nakajima, Combust. Flame, 140 (1-2) (2005) 34-45.
[11] M. De Leo, A. Saveliev, L.A. Kennedy, S.A. Zelepouga, Combust. Flame, 149 (4) (2007) 435-447.
[12] X. Song, Q. Guo, C. Hu, Y. Gong, G. Yu, Energy Fuels, 30 (2) (2016) 1428-1436.
[13] M. Smooke, Y. Xu, R. Zurn, P. Lin, J. Frank, M. Long, in: Symposium (International) on Combustion, Elsevier, 1992, pp. 813-821.
[14] J. Buckmaster, Prog. Energy Combust. Sci., 28 (5) (2002) 435-475.
[15] S.H. Chung, Proc. Combust. Inst., 31 (1) (2007) 877-892.
[16] K.M. Lyons, Prog. Energy Combust. Sci., 33 (2) (2007) 211-231.

[17] S. Lamige, J. Min, C. Galizzi, F. André, F. Baillot, D. Escudié, K.M. Lyons, Combust. Flame, 160 (6) (2013) 1102-1111.
[18] S. Lamige, K. Lyons, C. Galizzi, F. André, M. Kühni, D. Escudié, Exp. Therm Fluid Sci., 56 (2014) 45-52.
[19] L. Muniz, M. Mungal, Combust. Flame, 111 (1-2) (1997) 16-31.
[20] Y.-C. Chen, R.W. Bilger, Combust. Flame, 122 (4) (2000) 377-399.
[21] L. Su, O. Sun, M. Mungal, Combust. Flame, 144 (3) (2006) 494-512.
[22] J.E. Broadwell, W.J. Dahm, M.G. Mungal, in: Symposium (international) on combustion, Elsevier, 1985, pp. 303-310.
[23] N. Peters, F.A. Williams, AIAA J., 21 (3) (1983) 423-429.
[24] Y. Otakeyama, T. Yokomori, M. Mizomoto, Proc. Combust. Inst., 32 (1) (2009) 1091-1097.
[25] L. Vanquickenborne, A. Van Tiggelen, Combust. Flame, 10 (1) (1966) 59-69.
[26] C. Lawn, Prog. Energy Combust. Sci., 35 (1) (2009) 1-30.
[27] M. Bukar, S. Basnet, T. Kim, G. Magnotti, in: AIAA SCITECH 2022 Forum, 2022, pp. 0640.
[28] M. Marin, F. Baillot, Combust. Flame, 171 (2016) 264-280.
[29] L. Ding, A. Goshtasby, Pattern Recognit., 34 (3) (2001) 721-725.
[30] H.I. Joo, Ö.L. Gülder, Combust. Flame, 157 (6) (2010) 1194-1201.
[31] A.E. Karataş, Ö.L. Gülder, Fuel, 200 (2017) 76-80.
[32] H.I. Joo, Ö.L. Gülder, Proc. Combust. Inst., 32 (1) (2009) 769-775.
[33] M. Commodo, A.E. Karataş, G. De Falco, P. Minutolo, A. D'Anna, Ö.L. Gülder, Combust. Flame, 219 (2020) 13-19.
[34] K.A. Thomson, Ö.L. Gülder, E.J. Weckman, R.A. Fraser, G.J. Smallwood, D.R. Snelling, Combust. Flame, 140 (3) (2005) 222-232.
[35] S. Colson, M. Kuhni, A. Hayakawa, H. Kobayashi, C. Galizzi, D. Escudie, Combust. Flame, 234 (2021) 111657.